Numerical buckling analysis for flat and cylindrical shells including through crack employing effective reproducing kernel meshfree modeling

M. Ozdemir[a], S. Tanaka[b,*], S. Sadamoto[b,1], T.T. Yu[c], T.Q. Bui[d]

[a]*Department of Naval Architecture and Marine Engineering,*
Ordu University, Turkey, e-mail:muratozdemir@odu.edu.tr
[b]*Graduate School of Engineering, Hiroshima University, Japan,*
e-mail:satoyuki@hiroshima-u.ac.jp, shota.sadamoto@gmail.com
[c]*Department of Engineering Mechanics, Hohai University, China,*
e-mail: tiantangyu@hhu.edu.cn
[d]*Department of Civil and Environmental Engineering,*
Tokyo Institute of Technology, Japan, e-mail: bui.t.aa@m.titech.ac.jp

---

Abstract

Buckling behavior of flat and cylindrical shells including through-the-thickness crack (through crack) is examined employing an effective reproducing kernel (RK) meshfree method. The concept of convected coordinate system is adopted to deal with general curvilinear surfaces. Both field variables and shell geometry are approximated by RKs, which is conceptually same procedure with isoparametric Finite Element Method (FEM). Each node has five degrees of freedom (DOFs). The numerical integration of stiffness matrices is conducted by strain smoothing approaches. In the present study, a crack modeling is introduced into the curved shell geometry for analyzing cracked cylinder buckling problems effectively. The presented approach has an attractive feature, *i.e.*, five DOFs cracked flat shell model is only required for analyzing three-dimensional (3D) cracked curved shell problems. The accuracy and effectiveness of the present method are critically examined through several numerical examples in which the obtained results are compared with reference solutions as well as with the results of commercial FEM package

---

[*] Corresponding author

[1] Present address: Fujitsu Limited, 9-3, Nakase 1-chome, Mihama-ku, Chiba city, Chiba 261-8588, Japan.

(ANSYS). Effects of the element types in the FEM computations are also examined by comparison of the results by linear and quadratic shell elements. The results shed light on the significant effects of considered configurations on buckling coefficients and mode shapes.

Keywords: meshfree, reproducing kernel, cylindrical shell, buckling, crack

---

1. Introduction

Ship and offshore structures are often composed of plate and shell assemblies. They are usually designed in effective ways to provide higher structural performance during service life as well as for straightforward inspection and maintenance. The authors have studied buckling and ultimate strength of stiffened plate structures [1, 2] and ship's hull [3]. Some manufacturing operations such as welding or extreme variations in environmental conditions may generate defects, *e.g.*, through cracks, which might have detrimental effects on the integrity and load bearing capacity of the structures. These defects can sometimes be repaired by maintenance, however it is not always an easy task to inspect and alleviate the defects. It is therefore necessary to predict the performance and integrity of cracked structures. Buckling phenomenon is related with structural stability. Although, intact structures may buckle globally, buckling may take place locally near the crack due to higher stress gradients caused by discontinuity. Buckling phenomena are one of the main subjects to the scientific and engineering community, and they have been studied by many researchers using different approaches. This particular work however is devoted to the numerical buckling analysis of imperfect flat and cylindrical shells, but using a novel effective meshfree method.

Since last few decades, critical examination of cracked plates and shells has considerable interest employing analytical methods [4], semi-analytical methods [5, 6], experimental methods [7–9], FEM [10–19] and extended FEM (XFEM) [20–22]. Vafai and Estekanchi [10] conducted parametric FEM computations on the buckling of cracked plates and shells. Meshing pattern on the crack tip, boundary conditions (BCs), Poisson's ratio and shell curvature were considered as parameters affecting structural performance of the cracked flat and curved shells. Brighenti [13] studied the buckling behavior of thin plates under compressive and tensile loads. Aside to crack parameters, effect of Poisson's ratio was also examined since Poisson's ratio becomes a significant parameter under tensile loading condition. Khedmati *et al.* [15] carried out a series of parametric study to examine the effects of crack parameters on the buckling behavior of continuous ship plates. In the paper, crack location was also considered as a parameter affecting structural performance of the plate. Seifi and Khoda-yari [16] examined the buckling characteristics of central-inclined cracked plates conducting both experimental and numerical studies. Influences of crack length and orientation as well as plate thickness and edge conditions on the buckling behavior were examined. Estekanchi and Vafai [11] analyzed buckling problems of cylindrical shells under compression and tensile loads for different crack sizes and orientation angles. Special mesh zooming technique was employed on the crack tips instead of using special kind of tip elements. Then, Javidruzi *et al.* [12] considered fine mesh not only for crack tip but also crack segment for the both buckling and dynamic analysis of cracked cylindrical shells. It was also indicated that when the crack length is relatively small, the effect of fine mesh along crack segment becomes visible on buckling load. Buckling problems of cracked functionally graded cylindrical shells were recently addressed by Nasirmanesh and Mohammedi [22].

Based on the aforementioned facts, it could be said that the FEM was mainly adopted for the modeling and analysis of cracked shell structures. Linear shell elements are usually preferable for the modeling and analysis of ship and offshore structures owing to the less computational expense compared to higher order elements. On the other hand, adopting linear elements for the approximation and analysis of curvilinear surfaces may sometimes cause shear locking phenomenon. Fortunately, it is possible to see vital improvements in the element formulation and discretization, see Refs. [23, 24]. Meshfree methods and other related methods can overcome shear locking problems owing to higher order approximation functions. They are therefore popular for solving boundary value problems, *e.g.*, intact problems for isotropic [25–29]; composite [30–32] and functionally graded materials [33–35] and cracked problems [36–38] were handled. Isogeometric Analysis (IGA) [39] is recently emerged popular method and can be employed for predicting structural performance of the plates and shells [40–46]. As for the treatment of discontinuous problem domains, extended IGA (XIGA) [47, 48] can be employed. Nguyen-Thanh *et al.* [49] analyzed cracked Kirchhoff-Love curved shell employing XIGA.

In recent years, our research group carried out meshfree Reproducing Kernel Particle Method (RKPM) [50] buckling analyses for structural plates with curvilinear stiffeners by five DOFs flat shell formulation [51] and stiffened plates by six DOFs flat shell formulation [52]. Furthermore, buckling behavior of the cylindrical shells including circular cutouts with an efficient convected coordinate system was examined by present authors [53]. Convected coordinate system concept has been recently applied to the modeling and analysis of curvilinearly stiffened and complex shaped shells on the basis of six DOFs Mindlin-Reissner shell formulation [54]. RK meshfree formulation based on convected coordinate system with strain smoothing numerical integration techniques, *i.e.*, stabilized conforming nodal integration (SCNI) [55, 56] and sub-domain stabilized conforming nodal integration (SSCI) [57–61], is sometimes superior to conventional numerical methods so that a curvilinear geometry can be approximated effectively and shear locking can be avoided. Wang and Peng [59] proposed Hermite RK Galerkin method for the buckling analysis of thin plates employing SSCI, and superiority of the proposed method to the conventional Galerkin meshfree methods with Gauss quadrature was highlighted. Wang *et al.* [60] improved the previous concept for the buckling analysis of Kirchhoff-Love cylindrical shells. Wang and Wu [61] proposed nesting sub-domain gradient smoothing integration (NSGSI) based upon SSCI, and the stiffness matrix was integrated exactly for any quadratic field.

Although the present meshfree method has merits, *e.g.*, only five DOFs flat shell model is required for analyzing 3D cracked cylindrical shell problems, the problems have not been solved yet. Tanaka *et al.* [62–64] effectively applied diffraction method and visibility criterion [65, 66] for crack modeling in analyzing stress- and moment-intensity factors of cracked plane plate and shear deformable plate problems. So far, the modeling was adopted only for flat plate cases. We thus introduce crack modeling to the curvilinear surfaces on the basis of convected coordinates presented in [53] for analyzing cracked flat and cylindrical shell buckling problems. A singular kernel (SK) [67] is adopted for the cracked shell modeling and imposition of essential BCs. Several numerical examples for cracked flat and curved shells are presented and compared with existing solutions and FEM results. Effects of the element types are also investigated employing linear and quadratic shell elements for the FEM computations. The presence of crack to the shell structures are also discussed through the numerical results to investigate significance of defects in the structures for buckling coefficients and modes.

This paper is organized as follows. In Section 2, modeling of flat and curved shells in convected coordinates is briefly presented. We present effective meshfree modeling of cracks in Section 3. Discretization for linear buckling analysis is briefly explained in Section 4. Section 5 presents numerical examples of flat shells including cracks and circular cutouts, as well as cylinder models with cracks. Main conclusions are summarized in Section 6.

2. Modeling of flat and curved shells

The proposed technique is capable of transforming general 3D surface into the equivalent two-dimensional plane and vice-versa. The general shell is assumed to have a uniform thickness t_{h} throughout the analysis domain. A schematic illustration of the proposed mapping technique for Cartesian and convected coordinate system is shown in Fig.1. $\boldsymbol{X}=(X_1, X_2, X_3)$ is a position vector in the global Cartesian coordinate system, while $\boldsymbol{r}=(r_1, r_2, r_3)$ stands for a position vector in convected coordinates. RKs (nodes) on mid-thickness plane can be allocated in regular or irregular pattern. The physical values between two coordinates have one-to-one correspondence, *e.g.*, points *a*-*d* in Fig.1. The flat shell is a specific case of general curved shells.

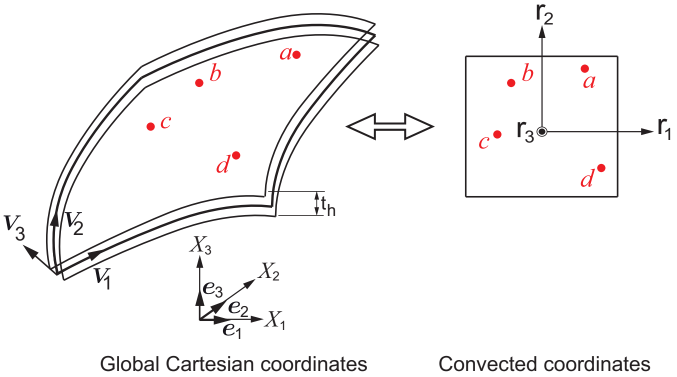

Figure 1: A schematic illustration of coordinate transformation between global Cartesian and convected coordinates.

2.1. Approximation of shell geometry and deformations

RKs are not only adopted for the curvilinear geometry interpolation, but also for the field variables approximation. The approximation scheme is same with the isoparametric FEM. The completeness condition can thus be met. Nodes can be randomly distributed on the mid-thickness plane as shown in Fig.1 and the orthogonal unit vector $\boldsymbol{V}_i$ is defined at each node; *i.e.*, $\boldsymbol{V}_{iI}$

for the I-th node. A position vector $\boldsymbol{X}_{\mathrm{mid}}(r_1, r_2)$ on the mid-thickness plane (r_1–r_2 plane) of the curved shell is interpolated using the RKs as:

$$\boldsymbol{X}_{\mathrm{mid}}(r_1, r_2) = \sum_{I=1}^{\mathrm{NP}} \psi_I(r_1, r_2)\boldsymbol{X}_{\mathrm{mid}I}, \tag{1}$$

where $\psi_I(r_1, r_2)$ and $\boldsymbol{X}_{\mathrm{mid}I}$ are the RK shape function and position vector of the I-th node on the mid-thickness plane, respectively. NP is the total number of scattered nodes used for the interpolation of the mid-thickness plane of the curved shell. The RK on the mid-thickness plane is $\psi_I(r_1, r_2)=\boldsymbol{h}^T(r_{1I} - r_1, r_{2I} - r_2)\boldsymbol{b}(r_1, r_2)\phi_I(r_{1I} - r_1, r_{2I} - r_2)$. Here $\boldsymbol{h}^T(r_{1I} - r_1, r_{2I} - r_2)$ and $\boldsymbol{b}(r_1, r_2)$ are the basis vector and coefficient vector, respectively. A complete quadratic basis is employed as the basis vector.

The displacement vector on mid-thickness plane can be approximated as:

$$\boldsymbol{u}_{\mathrm{mid}}(r_1, r_2) = \sum_{I=1}^{\mathrm{NP}} \psi_I(r_1, r_2)\boldsymbol{u}_{\mathrm{mid}I}. \tag{2}$$

Approximation of position $\boldsymbol{X}(r_1, r_2, r_3)$ and displacements $\boldsymbol{u}$ of a point on the general shell surface are accomplished by Eqs. (3) and (4), respectively, as follows.

$$\boldsymbol{X}(r_1, r_2, r_3) = \sum_{I=1}^{\mathrm{NP}} \psi_I(r_1, r_2)\left(\boldsymbol{X}_{\mathrm{mid}I} + \frac{r_3}{2} t_{\mathrm{h}} \boldsymbol{V}_{3I}\right), \tag{3}$$

$$\boldsymbol{u} = \left\{ \begin{array}{c} u_{\mathrm{mid}1} - \frac{t_{\mathrm{h}}}{2} r_3 \theta_1 V_{21} + \frac{t_{\mathrm{h}}}{2} r_3 \theta_2 V_{11} \\ u_{\mathrm{mid}2} - \frac{t_{\mathrm{h}}}{2} r_3 \theta_1 V_{22} + \frac{t_{\mathrm{h}}}{2} r_3 \theta_2 V_{12} \\ u_{\mathrm{mid}3} - \frac{t_{\mathrm{h}}}{2} r_3 \theta_1 V_{23} + \frac{t_{\mathrm{h}}}{2} r_3 \theta_2 V_{13} \end{array} \right\} = \sum_{I=1}^{\mathrm{NP}} \boldsymbol{\Psi}_I \boldsymbol{U}_I, \tag{4}$$

where θ_1 and θ_2 denote the rotation components on the mid-thickness plane with respect to unit vectors $\boldsymbol{V}_1$ and $\boldsymbol{V}_2$, respectively. V_{ij} (j=1,2,3) terms relate the rotation components to the global axes, and those terms can be computed by the dot products of unit vectors $\boldsymbol{V}_i$ and the unit vectors $\boldsymbol{e}_j$. $\boldsymbol{\Psi}_I$ is the displacement matrix in terms of RKs for the I-th node, which is written as:

$$\boldsymbol{\Psi}_I = \sum_{I=1}^{\mathrm{NP}} \left[\begin{array}{ccccc} \psi_I & 0 & 0 & -\frac{t_{\mathrm{h}}}{2} r_3 \psi_I V_{21} & \frac{t_{\mathrm{h}}}{2} r_3 \psi_I V_{11} \\ 0 & \psi_I & 0 & -\frac{t_{\mathrm{h}}}{2} r_3 \psi_I V_{22} & \frac{t_{\mathrm{h}}}{2} r_3 \psi_I V_{12} \\ 0 & 0 & \psi_I & -\frac{t_{\mathrm{h}}}{2} r_3 \psi_I V_{23} & \frac{t_{\mathrm{h}}}{2} r_3 \psi_I V_{13} \end{array} \right], \tag{5}$$

and $\boldsymbol{U}_I$ is coefficient vector of the I-th node, which is given by

$$\boldsymbol{U}_I = \left\{ \begin{array}{ccccc} u_{\text{mid}1I} & u_{\text{mid}2I} & u_{\text{mid}3I} & \theta_{1I} & \theta_{2I} \end{array} \right\}^T. \tag{6}$$

Covariant, $\boldsymbol{G}_i$=$\partial \boldsymbol{X}/\partial r_i$, basis vectors are defined for effective mapping operations as well as representing stress or strain tensors. Considering Eq. (3), the covariant basis vectors can be written as:

$$\begin{aligned} \frac{\partial \boldsymbol{X}}{\partial r_i} &= \sum_{I=1}^{\text{NP}} \frac{\partial \psi_I(r_1, r_2)}{\partial r_i} \left(\boldsymbol{X}_{\text{mid}I} + \frac{r_3}{2} t_{\text{h}} \boldsymbol{V}_{3I} \right), \quad (i = 1, 2), \\ \frac{\partial \boldsymbol{X}}{\partial r_3} &= \sum_{I=1}^{\text{NP}} \psi_I(r_1, r_2) \frac{1}{2} t_{\text{h}} \boldsymbol{V}_{3I}. \end{aligned} \tag{7}$$

In order to meet Kronecker Delta function property, contravariant bases, $\boldsymbol{G}^i$, are expressed as:

$$\boldsymbol{G}^i = \frac{\boldsymbol{G}_j \times \boldsymbol{G}_k}{\boldsymbol{G}_i \cdot (\boldsymbol{G}_j \times \boldsymbol{G}_k)}, \tag{8}$$

where (i, j, k)=(1,2,3),(2,3,1),(3,1,2).

3. Meshfree modeling of a through crack

A through crack embedded in a curved shell is presented in Fig.2(a). In the figure, c is the crack length, while S_c represents the crack segment. When analyzing the cracked curved shell, a cracked rectangular plate is arranged and a mapping technique is adopted through convected coordinate system as shown in Fig.2(b). This is an effective way to generate cracked curved shell geometries because meshfree interpolants are only defined in the local coordinate system, $\boldsymbol{r}$=(r_1, r_2, r_3).

Meshfree modeling of crack tip and crack segment, respectively, by diffraction method and visibility criteria [65, 66] on the local coordinate system $\boldsymbol{r}$=(r_1, r_2, r_3) is schematically illustrated in Fig.3(a). The crack tip is represented by a node, and the crack segment is modeled by an assembly of double nodes. r_1' and r_2' are local coordinates from the crack tip, and (ρ,φ) denotes the location of a point in the local polar coordinates with respect to crack tip node as indicated in Fig.3(b). D_+/D_- denotes upper/lower regions of the crack segment, $\boldsymbol{r}_c$ is a crack tip node. When including the crack tip node $\boldsymbol{r}_c$

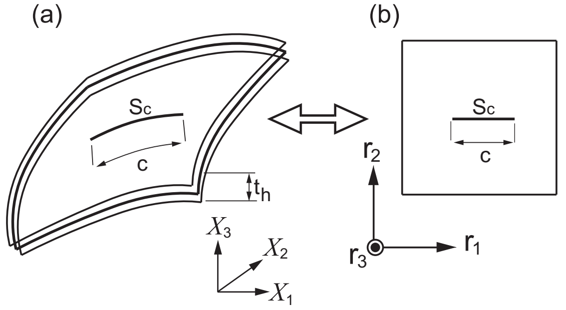

Figure 2: Crack modeling: (a) global Cartesian coordinates, (b) convected coordinates.

within the function support of the node $\boldsymbol{r}_I$, the diffraction method is adopted. The normalized distance d_I in the original kernel ϕ_I of Eq. (10) is revised as $\hat{d}_I$ to treat the displacement discontinuity across the crack segment:

$$\hat{d}_I = \left(\frac{d_1 + s_2(\boldsymbol{r})}{d_0(\boldsymbol{r})}\right)^{\mu} \frac{d_0(\boldsymbol{r})}{h_I}, \tag{9}$$

where $d_0(\boldsymbol{r})=||\boldsymbol{r} - \boldsymbol{r}_I||$, $d_1=||\boldsymbol{r}_c - \boldsymbol{r}_I||$, and $d_2(\boldsymbol{r})=||\boldsymbol{r} - \boldsymbol{r}_c||$ are normalized distances. The shape parameter μ is taken as 1.0. In representing the displacement discontinuity along the crack segment, the RKs are completely or partially cut by the crack segment. If a node $\boldsymbol{r}_J$ belongs to domain D_+, numerical integration of the stiffness matrix in terms of node $\boldsymbol{r}_J$ is partially carried out for domain D_+. SSCI [57–61] is introduced to perform numerical integrations around the cracks as shown in Fig.3(c). In Fig.3(c), the boundaries of Voronoi cells for SCNI are represented by solid lines, while the boundaries of triangular sub-domains for SSCI are represented by dashed red lines. When introducing an RK around the crack tip, an enriched term to simulate singular stress field at crack tip is included in the basis vector, $\boldsymbol{h}(\boldsymbol{r})=\{1 \;\; r_1 \;\; r_2 \;\; (r_1)^2 \;\; r_1 r_2 \;\; (r_2)^2 \;\; \sqrt{\rho}\sin(\varphi/2)\}$. The enriched basis vector is adopted only for the quadrature points within the function support of $\boldsymbol{r}_c$.

A schematic illustration for densely scattered nodes towards point "A" is given in Fig.4. The distance between two nodes gradually decreases towards point "A". A control parameter α_I is adopted, (*i.e.*, $h_I=\alpha_I h_I^p$), and the RKs are developed. α_I is assumed to be constant as 1.3 for uniform nodal distribution, while α_I is varied between 1.25 and 1.35 for the support size of the nodes near cracks. h_I^p is the characteristic length for the I-th node. Cubic spline function is adopted as original kernel function with variable function

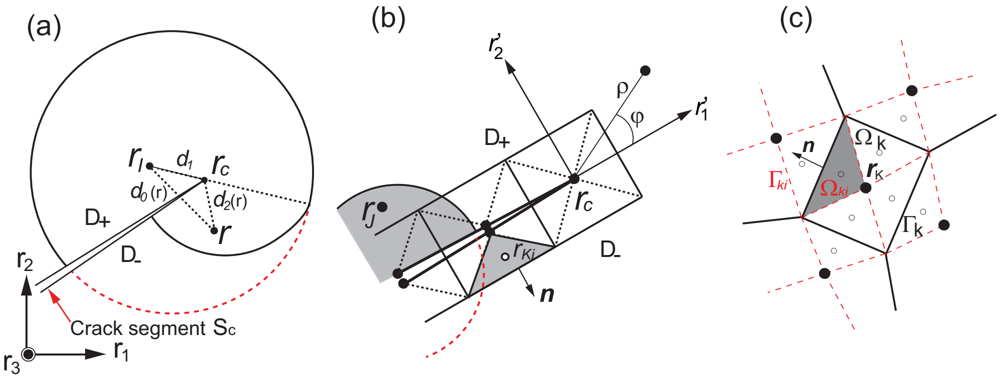

Figure 3: Crack modeling by RK meshfree method: (a) diffraction method and visibility criterion, (b) local polar coordinates and Voronoi cells, (c) SCNI and SSCI for the crack modeling.

support control parameter h_I to control the nodal density as:

$$\phi_I = \frac{10}{7\pi h_I^2} \left\{ \begin{array}{cc} 1-\frac{3}{2}d_I^2+\frac{3}{4}d_I^3 & (0 \le d_I \le 1) \\ \frac{1}{4}(2-d_I)^3 & (1 \le d_I \le 2) \\ 0 & (2 \le d_I) \end{array} \right. , \tag{10}$$

where d_I=$\sqrt{(r_{1I}-r_1)^2+(r_{2I}-r_2)^2}/h_I$, which represents the normalized distance from the center of the kernel. The crack modeling is introduced for both approximation of physical values and curved shell geometries.

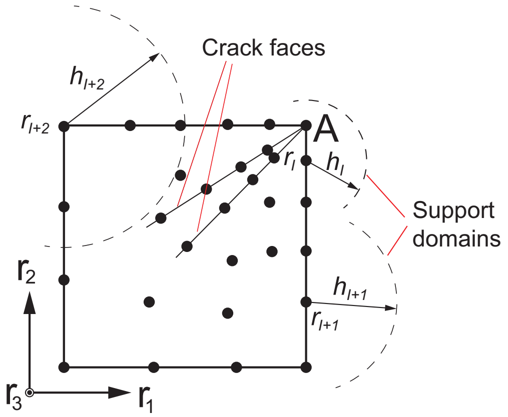

Figure 4: A schematic illustration for the control of nodal density in the meshfree modeling.

4. Linear buckling analysis

The weak form of the buckling problems can be written as:

$$\int_V \boldsymbol{\sigma} : \delta\boldsymbol{\varepsilon}_{\mathrm{L}} dV + \lambda \int_V \boldsymbol{\sigma}_0' : \delta\boldsymbol{\varepsilon}_{\mathrm{NL}} dV = 0, \tag{11}$$

where $\boldsymbol{\varepsilon}_{\mathrm{L}}$ and $\boldsymbol{\varepsilon}_{\mathrm{NL}}$ are the linear and nonlinear components of strain tensor, respectively. $\boldsymbol{\sigma}$ and $\boldsymbol{\sigma}_0'$ represent, respectively, the Cauchy stress tensor and pre-buckling stress tensor. λ is the buckling factor.

The linear and nonlinear components of total strain are given as:

$$\begin{aligned}\boldsymbol{\varepsilon} &= \frac{1}{2}\left\{\left(\boldsymbol{G}_i \cdot \frac{\partial \boldsymbol{u}}{\partial r_j} + \boldsymbol{G}_j \cdot \frac{\partial \boldsymbol{u}}{\partial r_i}\right) + \left(\frac{\partial \boldsymbol{u}}{\partial r_i} \cdot \frac{\partial \boldsymbol{u}}{\partial r_j}\right)\right\}\boldsymbol{G}^i \otimes \boldsymbol{G}^j \\ &= \left(\varepsilon_{\mathrm{L}ij} + \varepsilon_{\mathrm{NL}ij}\right)\boldsymbol{G}^i \otimes \boldsymbol{G}^j = \boldsymbol{\varepsilon}_{\mathrm{L}} + \boldsymbol{\varepsilon}_{\mathrm{NL}}. \end{aligned} \tag{12}$$

Components of linear strain matrix are expressed as:

$$\varepsilon_{\mathrm{L}ij} = \sum_{I=1}^{\mathrm{NP}} \begin{bmatrix} \boldsymbol{G}_1^T \boldsymbol{\Psi}_{I,1} \\ \boldsymbol{G}_2^T \boldsymbol{\Psi}_{I,2} \\ \boldsymbol{G}_1^T \boldsymbol{\Psi}_{I,2} + \boldsymbol{G}_2^T \boldsymbol{\Psi}_{I,1} \\ \boldsymbol{G}_2^T \boldsymbol{\Psi}_{I,3} + \boldsymbol{G}_3^T \boldsymbol{\Psi}_{I,2} \\ \boldsymbol{G}_3^T \boldsymbol{\Psi}_{I,1} + \boldsymbol{G}_1^T \boldsymbol{\Psi}_{I,3} \end{bmatrix} \boldsymbol{U}_I = \sum_{I=1}^{\mathrm{NP}} \boldsymbol{B}_{\mathrm{L}I} \boldsymbol{U}_I, \tag{13}$$

where $\boldsymbol{B}_{\mathrm{L}I}$ is the displacement-linear strain matrix and $\boldsymbol{\Psi}_{I,i}$ denotes the derivative of the displacement matrix $\boldsymbol{\Psi}_I$ in Eq. (5). As for the components of the displacement-nonlinear strain matrix, $\boldsymbol{B}_{\mathrm{NL}I}$, the vector $\boldsymbol{d}^T$ is described as:

$$\boldsymbol{d}^T = \left\{ \left(\frac{\partial \boldsymbol{u}}{\partial r_1}\right)^T \left(\frac{\partial \boldsymbol{u}}{\partial r_2}\right)^T \left(\frac{\partial \boldsymbol{u}}{\partial r_3}\right)^T \right\}. \tag{14}$$

We finally arrive the relation between $\boldsymbol{d}$ and $\boldsymbol{B}_{\mathrm{NL}I}$ as below.

$$\boldsymbol{d} = \sum_{I=1}^{\mathrm{NP}} \begin{bmatrix} \boldsymbol{\Psi}_{I,1} \\ \boldsymbol{\Psi}_{I,2} \\ \boldsymbol{\Psi}_{I,3} \end{bmatrix} \boldsymbol{U}_I = \sum_{I=1}^{\mathrm{NP}} \boldsymbol{B}_{\mathrm{NL}I} \boldsymbol{U}_I, \tag{15}$$

Substituting Eqs. (13) and (15) into Eq. (11) and considering the stress–strain relationship for linear elastic material model, a discrete equation of the eigenvalue problem is then derived as:

$$(\boldsymbol{K}_{\mathrm{L}} + \lambda \boldsymbol{K}_{\mathrm{NL}})\boldsymbol{U} = 0, \tag{16}$$

where $\boldsymbol{K}_{\mathrm{L}}$ and $\boldsymbol{K}_{\mathrm{NL}}$ are stiffness matrices associated with linear and nonlinear terms, respectively. $\boldsymbol{K}_{\mathrm{L}}$ is the global stiffness matrix, and it is only a function of model geometry and material properties. On the other hand, $\boldsymbol{K}_{\mathrm{NL}}$, which is also referred to as stress stiffness or geometric stiffness matrix, is a function of loading, and so the pre-buckling stresses, as well as the model. $\boldsymbol{K}_{\mathrm{L}}$ and $\boldsymbol{K}_{\mathrm{NL}}$ matrices are respectively given as:

$$\boldsymbol{K}_{\mathrm{L}} = \int_V \boldsymbol{B}_{\mathrm{L}}^T \boldsymbol{C} \boldsymbol{B}_{\mathrm{L}} dV, \tag{17}$$

$$\boldsymbol{K}_{\mathrm{NL}} = \int_V \boldsymbol{B}_{\mathrm{NL}}^T \boldsymbol{\sigma}_0' \boldsymbol{B}_{\mathrm{NL}} dV, \tag{18}$$

where $\boldsymbol{C}$ stands for the linear elastic stress-strain matrix of the material, and the components of $\boldsymbol{C}$ were already given in Ref. [53].

4.1. Numerical integration techniques

Stiffness matrices are derived by employing SCNI [55, 56] and SSCI [57-61]. Higher stress gradients along the crack segment as well as the crack tip are effectively captured by SSCI. SCNI is adopted for the remaining parts of the models. Numerical integration domains, Voronoi cells, enclosing the nodes/kernels, are allocated for SCNI. Strain components include the partial derivatives of displacements and so the partial derivatives of the kernel functions. By applying the Gauss' divergence theorem to the partial differential term of displacement, $\tilde{d}_{i,j}^h$, the domain integral can be transformed to the contour integral as follows.

$$\begin{aligned} \tilde{d}_{i,j}^h(\boldsymbol{r}_K) &= \frac{1}{A_K} \int_{\Omega_K} d_{i,j}^h(\boldsymbol{r})\, d\Omega \\ &= \frac{1}{A_K} \int_{\Gamma_K} d_i^h(\boldsymbol{r}) n_j \, d\Gamma = \sum_{I=1}^{\mathrm{NP}} b_{Ij}(\boldsymbol{r}_K) d_{iI}, \end{aligned} \tag{19}$$

where i=$\{1, 2, 3, 4, 5\}$, j=$\{1, 2\}$ and

$$b_{Ik}(\boldsymbol{r}_K) = \frac{1}{A_K} \int_{\Gamma_K} \Psi_I(\boldsymbol{r}) n_k \, d\Gamma. \tag{20}$$

In Eq. (19), ($\tilde{}$) stands for smoothed values. A_K is area of the domain, Ω_K as shown in Fig.3(c).

SSCI, which is an extension of SCNI by further dividing SCNI domains, Ω_K into triangular sub-domains, Ω_{Ki} as shown in Fig.3(c), is adopted for simulating higher stress gradients around the cracks. In the sub-domains, any physical quantity can be smoothed as:

$$\begin{aligned} \tilde{d}_j^h(\boldsymbol{r}_{K_i}) &= \frac{1}{A_{K_i}} \int_{\Omega_{K_i}} d_j^h(\boldsymbol{r}) \; d\Omega \\ &= \sum_{I=1}^{\mathrm{NP}} \frac{1}{A_{K_i}} \int_{\Omega_{K_i}} \Psi_I(\boldsymbol{r}) d_{jI} \; d\Omega. \end{aligned} \tag{21}$$

In Eq. (21), A_{K_i} represents area of the sub-domains. As similar to Eq. (19), the derivatives of the displacement components, $\tilde{d}_{j,k}(\boldsymbol{r}_{K_i})$, can be obtained by:

$$\tilde{d}_{j,k}^h(\boldsymbol{r}_{K_i}) = \sum_{I=1}^{\mathrm{NP}} b_{Ik}(\boldsymbol{r}_{K_i}) d_{jI}, \tag{22}$$

where j=$\{1,2,3,4,5\}$, k=$\{1,2\}$ and

$$b_{Ij}(\boldsymbol{r}_{K_i}) = \frac{1}{A_{K_i}} \int_{\Gamma_{K_i}} \Psi_I(\boldsymbol{r}) n_j \; d\Gamma, \quad j = \{1,2\}, \tag{23}$$

where Γ_{K_i} represents boundary of the sub-domains, and see Fig.3(c). Although numerical integration along plate thickness direction can be carried out analytically, Newton-Cotes formula is adopted for the numerical integration for through-thickness direction in the meshfree computations.

5. Numerical examples and discussions

Buckling loads/modes for flat shells including cracks and cutouts, as well as for cylindrical shells including cracks are presented. Meshfree results are compared with those of FEM computations and available reference solutions. Central cracks are considered and crack length, as well as the crack orientation angle, are varied. When the crack size is relatively small compared to the whole problem domain, the nodal density is increased towards crack zone as shown in Fig.5. The crack tip is located on a node and double nodes are generated on the crack segment. SSCI and SCNI methods are adopted for the numerical integration around the crack segment and remaining parts, respectively as shown in Fig.5.

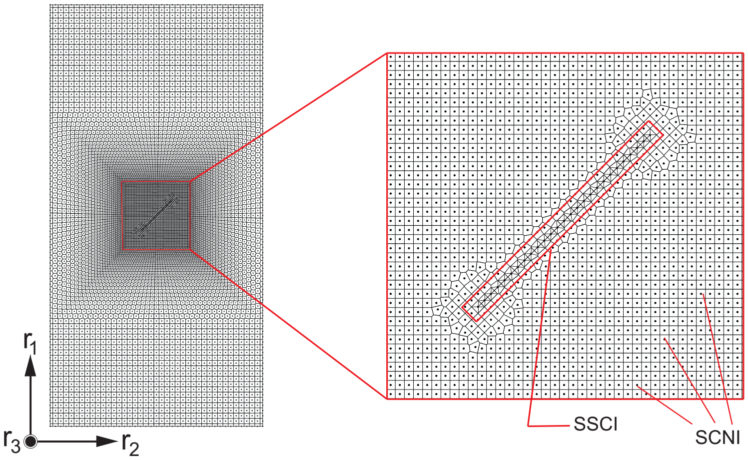

Figure 5: Representative meshfree model of a cracked flat shell.

Obtained buckling loads/modes are compared with fully converged results of FEM and reference results. The commercial FEM package ANSYS [68], which offers several shell element options, is used. In particular, the four-noded linear shell elements (Shell181) and eight-noded quadratic shell elements (Shell281) are considered, and their corresponding results of buckling are then reported for the comparison purpose. Both type of elements consider transverse shear deformation on the basis of Reissner-Mindlin theory. Linear elements have the capability of modeling flat surfaces in a high level of precision; however, as for the modeling of curvilinear surfaces as well as for the representation of sharper deformations near the cracks, assembly of flat shell elements may not be appropriated to describe the geometry and buckling deformation precisely. Then, only linear elements are adopted for the modeling of flat shell models. On the other hand, both type of elements are employed in the modeling of curvilinear surfaces to examine the effects of element formulations and the representation of buckling deformations near the discontinuities.

The main purpose of this study is to investigate the buckling behavior of flat and cylindrical shells by FEM and proposed meshfree method. Particular attention is therefore given to simulate sharp buckling deformations along the crack segment, but not to examine fracture mechanics parameters. This is the reason why we adopt fine mesh/nodal distribution not only for crack tip but also crack segment.

5.1. Buckling analysis of cracked flat shells

The shell models adopted from Ref. [13] are thus considered to validate the present meshfree method. In the reference paper, fine mesh is considered only for crack tips, however fine mesh must be adopted not only for the crack tip but also for the crack segment in case of flat shells with relatively small cracks. In this respect, nodal density is increased towards the cracks in the present computations. Simply supported BCs are assumed for all edges so as to free in-plane deformation of the flat shell. Then, critical buckling load factors are non-dimensionalized with elastic buckling load of intact flat shell. Elastic buckling load of simply supported plate, σ_E^{cr}, under longitudinal compression is calculated as [69]:

$$\sigma_E^{cr} = \frac{\pi^2 t_\mathrm{h}^2 E}{12(1-\nu^2)W^2}\left(\frac{L}{mW}+\frac{mW}{L}\right)^2, \tag{24}$$

where E and ν are Young's modulus and Poisson's ratio, respectively. m denotes buckling half wave number in load direction. Other parameters are indicated in Fig.6. The buckling coefficient, $L_\mathrm{c}=\sigma/\sigma_E^{cr}$, is adopted in order to present the results. Here, σ denotes buckling load of cracked flat shell. For the intact model, the non-dimensional buckling coefficient is $L_\mathrm{c}=1.0$. Material properties are assumed as $E=70{,}000$ MPa and $\nu=0.3$. The aspect ratio is $L/W=2.0$, while the shell thickness is taken as $t_\mathrm{h}/W=1/400$. In Fig.6, the crack orientation angle θ is varied as 0°, 15°, 30°, 45°, 60°, 75° and 90°. Five different crack sizes are considered as $c/W=0.1$, 0.2, 0.3, 0.4 and 0.5. Node distance is assumed as $W/40$ on the edges of the meshfree models. Nodal density is then increased towards the crack segment.

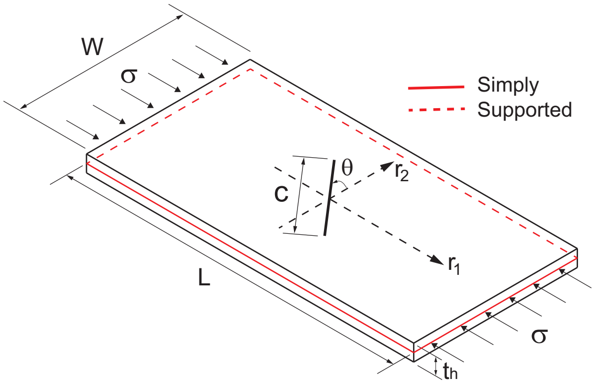

Figure 6: Representative flat shell model with a central crack.

As for the FEM models, linear shell elements (Shell181) are adopted. Then, mesh convergence is studied for a particular case, which is c/W=0.5, θ=45°. Fig.7 indicates the mesh convergence results of FEM computations for the cracked flat shell models. Total number of nodes np is increased gradually, buckling coefficients L_c are then obtained as shown in Fig.7(a). The buckling coefficient for the finest mesh is assumed to be fully converged result. In Fig.7(b), the errors for relatively coarse finite element meshes with respect to fully converged FEM result (reference value) are computed and plotted on logarithmic scale. In the figure, the error is defined as:

$$Error(\%) = 100 \times \frac{|L_\mathrm{c}^{coarse} - L_\mathrm{c}^{ref}|}{L_\mathrm{c}^{ref}}, \tag{25}$$

where L_c^{coarse} and L_c^{ref} represent the buckling coefficients for coarser meshes and reference buckling coefficient, which is obtained by the finest mesh.

Buckling coefficients for critical modes by FEM and present meshfree method are compared. The maximum difference among all the cases occurs for c/W=0.5, θ=45°, which is 0.43% of the fully converged FEM result. Total numbers of nodes np are 3,316 and 13,606 for meshfree and FEM models, respectively. It could be said that the agreement between the present formulation and FEM is excellent. Furthermore, the numerical results of critical buckling loads for all crack size and crack orientation angles calculated by the present meshfree method (MFree) are depicted in Fig.8. In the figure, lines with different colors indicate the reference results derived from different approaches of FEM. One must be noticed to the reference results given in Fig.8 that ones taken from Ref. [13] were obtained by finite element package

Strand7, whereas other FEM results are obtained by ANSYS, performed by the authors. In addition, Meshfree and FEM results are denoted by different type of markers and different colors.

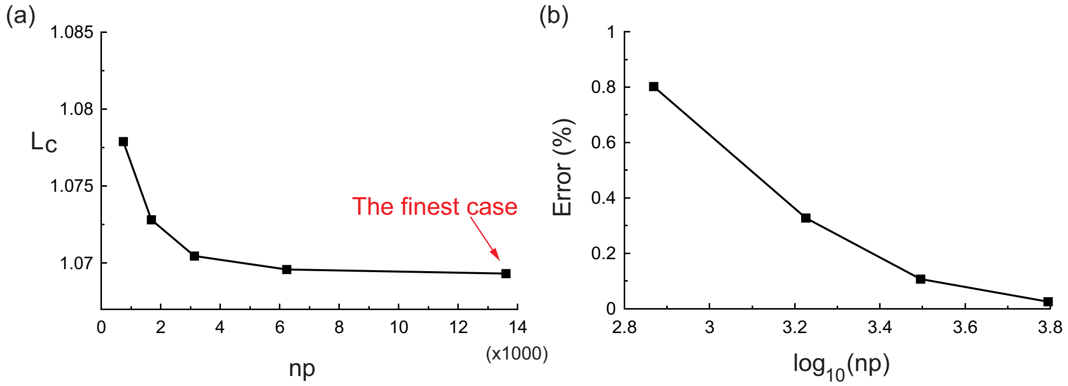

Figure 7: Convergence study for FEM (c/W=0.5, θ=45° case).

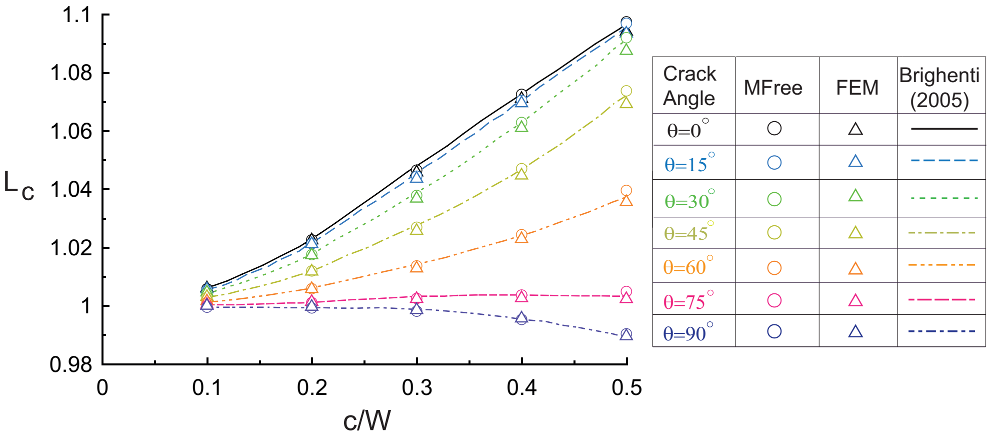

Figure 8: Comparison of results for proposed technique with those of FEM and Ref. [13].

In Fig.8, the effect of crack orientation angle on the critical buckling loads of cracked flat shells is significant. It is then found that when crack segment is in the same direction with the compressive loads (θ=90°), the critical buckling load is almost same with that of intact flat shell when the crack size is relatively small. On the other hand, a decrease of the crack orientation

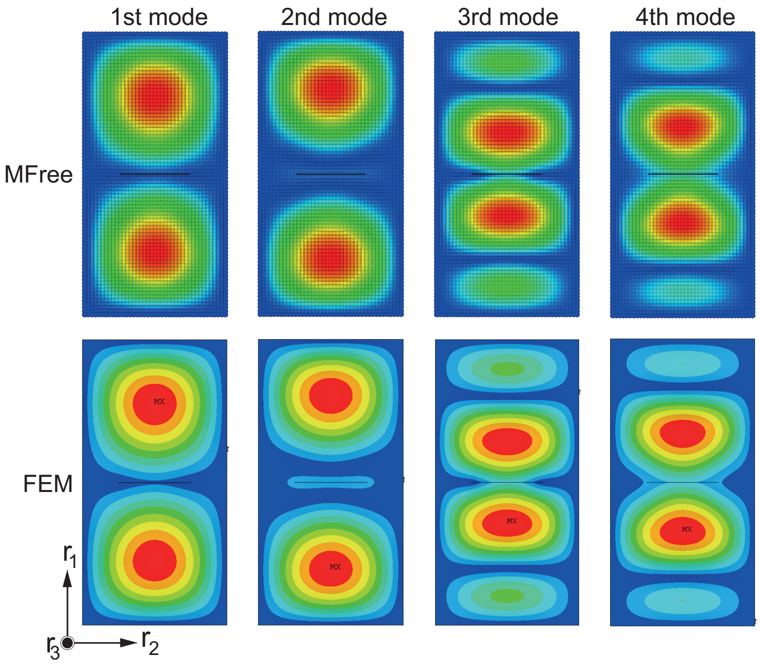

Figure 9: 1st–4th buckling modes for c/W=0.5, θ=0°.

angle, with respect to r_2-axis, the critical buckling load of the flat shells increases. In addition, the effect of crack size is investigated. When the crack segment and load direction is perpendicular to each other, the critical buckling load is increased with increasing the crack length, while if the crack segment and load is parallel to each other, the critical buckling load reduces slightly with increasing the crack size.

1st–4th buckling loads/modes obtained by FEM and proposed method are also examined, and their corresponding results are then shown in Tables 1 and 2 as well as Figs.9 and 10. It is observed that the present technique is capable of calculating critical buckling loads as well as higher order loads and modes. The higher order buckling mode shapes for the largest crack case shown in Figs.9 and 10 are particularly considered for θ=0° and 90°, respectively. Results reported in Tables 1, 2 and Figs.9, 10 clearly indicate a very good agreement between two considered solutions, reflecting the high accuracy of the present meshfree formulation and discretization. In the case of parallel crack segment to the load direction, stress streamlines are not disturbed by the existence of crack. This may cause the almost same buckling coefficients

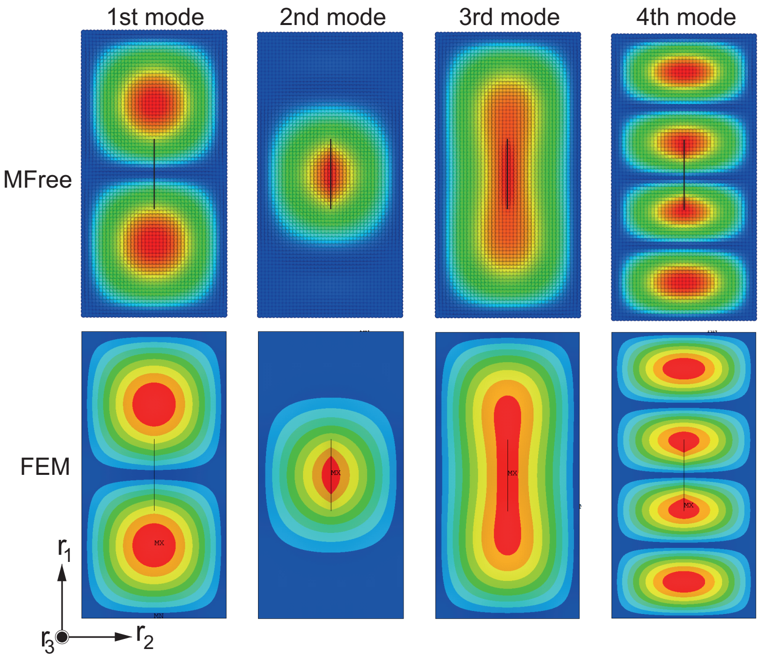

Figure 10: 1st–4th buckling modes for c/W=0.5, θ=90°.

with and without crack cases. On the other hand, the existence of cracks normal to the load direction disturbs the continuity of stress streamlines. In addition, critical buckling mode shape, which is two half-wave mode, is not affected by the existence of cracks. Bending moment becomes zero on the central part of the intact models when buckling occurs in two half-wave mode. However, the bending moment in central part of model would not be zero due to the existence of crack, which is normal to the stress streamlines. This could be the reason of higher buckling loads of cracked flat shells compared to intact cases.

Table 1: Comparison for 1st–4th buckling coefficients L_c of cracked flat shells (c/W=0.1).

	θ=0°		θ=90°	
Mode	MFree	FEM	MFree	FEM
1st	1.006	1.006	1.000	1.000
2nd	1.173	1.174	1.169	1.170
3rd	1.574	1.575	1.546	1.548
4th	1.583	1.582	1.562	1.564

Table 2: Comparison for 1st–4th buckling coefficients L_c of cracked flat shells (c/W=0.5).

	θ=0°		θ=90°	
Mode	MFree	FEM	MFree	FEM
1st	1.098	1.094	0.990	0.990
2nd	1.171	1.167	1.036	1.029
3rd	1.839	1.812	1.339	1.335
4th	2.093	2.085	1.543	1.542

Table 3: Comparison for higher order buckling coefficients L_c of cutout flat shells with and without cracks.

	c/W=0 (only cutout)		c/W=0.05 (crack and cutout)			
			θ=0°		θ=90°	
Mode	MFree	FEM	MFree	FEM	MFree	FEM
1st	1.063	1.063	1.083	1.093	1.067	1.070
2nd	1.098	1.099	1.128	1.147	1.089	1.079
3rd	1.516	1.517	1.578	1.631	1.499	1.482
4th	1.613	1.617	1.664	1.686	1.612	1.613

Next step is to analyze more complex problems for the crack flat shells. Cracks are set to be located at the edge of a circular cutout. Only one crack size, which is located normal and parallel to load direction, is analyzed. The radius of circular cutout is assumed as $W/8$. The crack size is taken as c/W=0.05. Model dimensions and material properties are same as previous numerical examples. The computed results are given in Table 3. In the table, buckling coefficients are given for the cases of cutout flat shells with and without cracks. When the crack orientation is parallel to load direction (θ=90°), the buckling coefficients for cutout shells with and without crack cases are almost same. On the other hand, if the crack orientation is normal to the load direction (θ=0°), the existence of crack produces extra bending moments on the central part of cutout shell causing higher buckling loads compared to without crack case. Critical buckling mode shapes for cutout flat shells with vertical (θ=0°) and horizontal (θ=90°) cracks are demonstrated in Fig.11(a) and (b), respectively. Good agreement is obtained between proposed technique and FEM in terms of critical mode shapes.

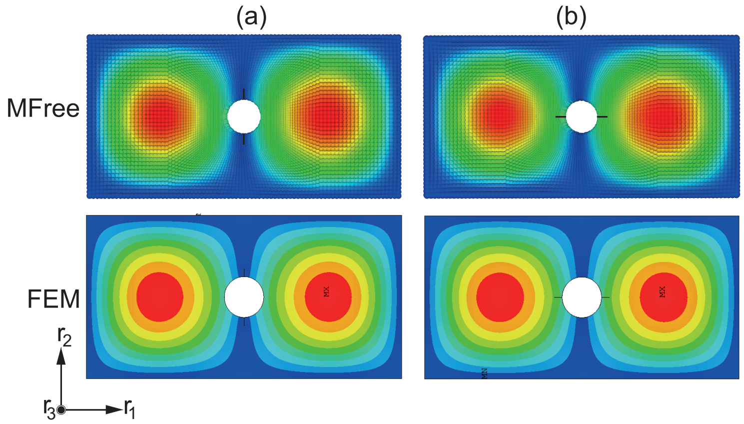

Figure 11: Critical buckling mode shapes for cutout shells with cracks: (a) θ=0°, (b) θ=90°.

5.2. Buckling analysis of cracked cylinders

Buckling analysis of cracked cylinders are carried out to examine the effects of crack size and orientation on both buckling loads and mode shapes as well as to show capability of the present meshfree formulation and discretization. The concept of convected coordinate system is introduced in order to model curvilinear surfaces. A flat shell model with a crack as shown in Fig.12(a), which is similar to previous numerical examples, is firstly generated; the cylinder models are then obtained by mapping as seen in Fig.12(b). After mapping operation, all DOFs of the overlapped nodes are tied. For the tying operation, SKs are imposed to the overlapped nodes to meet Kronecker Delta property. However, the authors sure that Kronecker Delta property by SKs can be imposed only to the nodes but not between the nodes, which may reduce the accuracy in the meshfree formulation. Fortunately, allocating enough number of nodes along the longitudinal direction of the cylinders would reduce the numerical error caused by the incompatible approximation of the overlapped edges. Moreover, Wang *et al.* [60] and Chen and Wang [70] addressed incompatible approximation between the patches, which sheds light on how to overcome such drawback of SK method as a future work. Again, it is noted that the meshfree modeling is very simple and effective for analyzing crack cylinder problems because flat plate model is only required.

Examples for numerical computations are adopted from Ref. [12]. Only three sizes of cracks, which correspond to relatively small and intermediate and large sizes, are considered. Obtained critical buckling loads, as well as

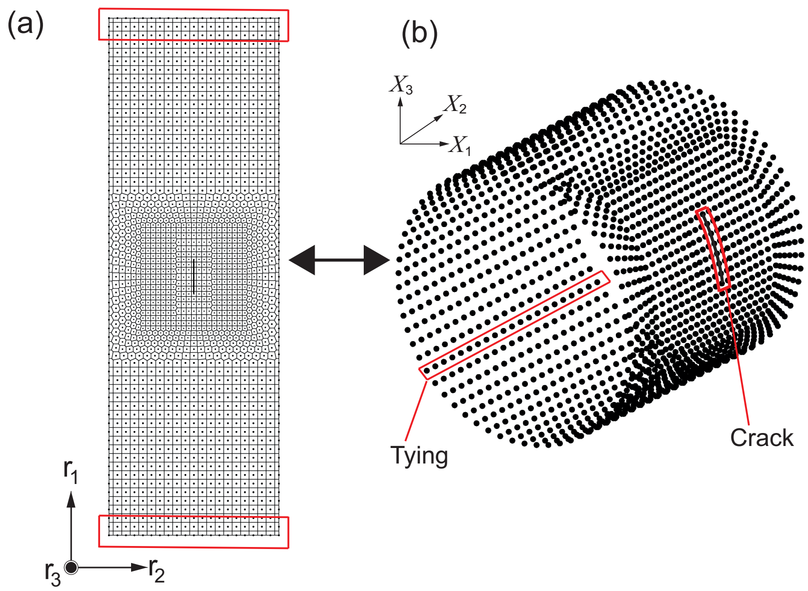

Figure 12: Meshfree modeling of cracked cylinders: (a) flat shell model, (b) cylinder model.

mode shapes, are compared with those of both reference paper and FEM. For now, circumferential and axial cracks with different sizes under axial compression are considered. Different crack orientation angles and crack sizes could be considered as a future work. Geometric properties and material properties are the same as [12]. E and ν are taken as 70,000 MPa and 0.35, respectively. Cracked cylinder models are schematically illustrated in Fig.13(a) and (b) for circumferential and axial cracks, respectively. Cylinder's length L, radius of the cylinder r_{d} and shell thickness t_{h} are taken as 1,000 mm, 500 mm and 1.0 mm, respectively.

Numerical computations are performed under fully clamped BCs setting the displacements free along the cylinder longitudinal axis. Both sided compression load is applied. It is known that local buckling takes place near the cracks so that the effect of BCs on the critical buckling mode and load becomes small. Critical buckling load of cracked cylinders is thus normalized with that of the intact simply supported cylinder as $L_k{=}P/\sigma^c_{\mathrm{cr}}$. L_k is the normalized buckling coefficient for cracked cylinder models, while σ^c_{cr} is the buckling stress of the simply supported intact cylinder, and it is readily obtained by $\sigma^c_{\mathrm{cr}}{=}Et_{\mathrm{h}}/r_{\mathrm{d}}\sqrt{3(1-\nu^2)}$. Cylindrical shells with circumferential cracks are represented by "CC1", "CC2" and "CC3", which correspond to

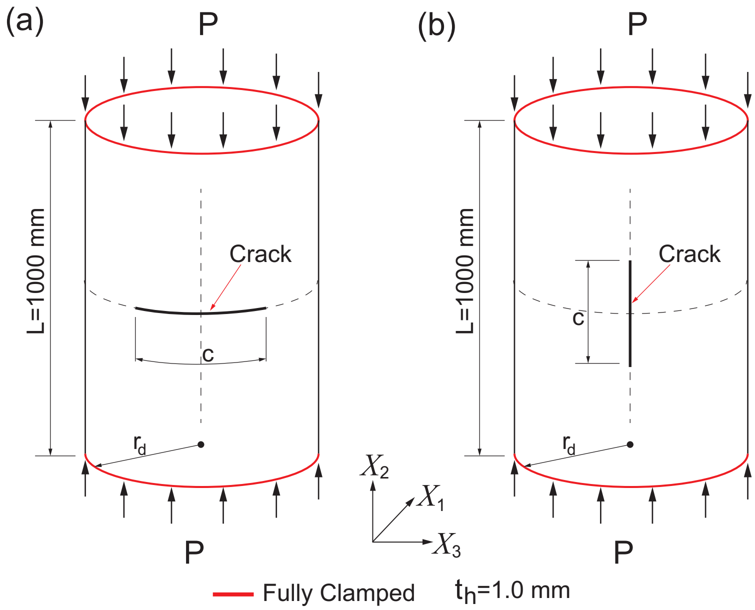

Figure 13: Illustration of cracked cylinder models: (a) circumferential crack, (b) axial crack.

$c/2\pi r_\mathrm{d}$=0.05, 0.10, 0.15 cases, respectively. In a similar fashion, the axial crack models are represented by "AC1", "AC2" and "AC3", which denote the c/L=0.05, 0.10 and 0.15 cases, respectively. Fully converged solutions with very fine mesh are adopted for FEM results, while nodal distance in the meshfree model is assumed as $L/40$ on the edges and nodal density is increased towards the crack based on the observations from our previous work [53]. Mesh convergence is studied for FEM computations considering two different shell element formulations, namely, linear (Shell181) and quadratic (Shell281) elements for a particular case, which is "AC2". Critical buckling takes place along the crack segment in a single half-wave mode for AC2 model, and the element sizes/numbers along the crack must be studied to obtain accurate buckling loads and modes. Element edge length γ along the crack segment is varied as 25, 20, 15, 10 mm for both element types.

The convergence study is demonstrated in Fig.14. In Fig.14(a), change of buckling coefficients L_k is examined with respect to np. When the element edge length, γ is 10 mm, almost the same buckling coefficients are obtained for linear and quadratic shell elements. In these cases, total numbers of nodes are 32,660 and 27,089 for linear and quadratic elements, respectively. Then, the buckling coefficient obtained by quadratic elements with the finest mesh is adopted as reference value for the error computation. Error computation is performed by Eq. (25) and it is plotted with respect to element edge length, γ, along the crack segment in Fig.14(b) using logarithmic scale. In the figure, element edge lengths are considered as 25, 20 and 15 mm since the reference value in the error computation is obtained by setting element edge length, γ along the crack as 10 mm.

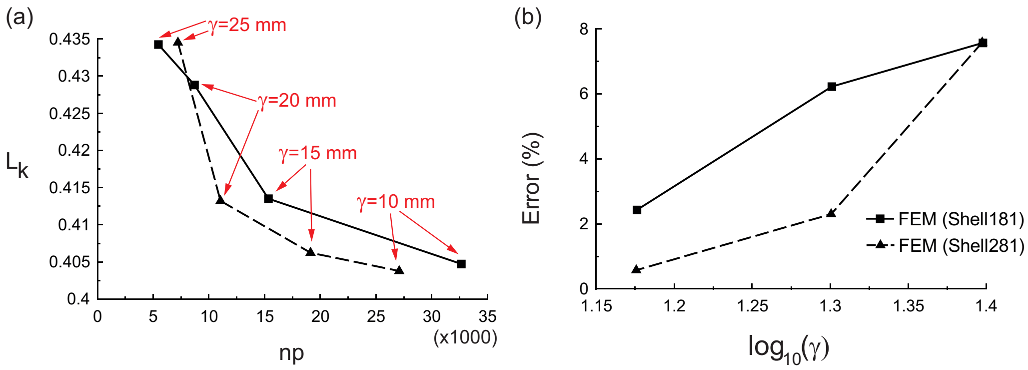

Figure 14: Convergence study for FEM (AC2 case): (a) Convergence with respect to np, (b) error with respect to element edge length γ along the crack.

Cracked cylinder problems are studied by present meshfree formulation and discretization as well as FEM varying the crack size and crack orientation. The effect of element formulation on modeling and analysis of curvilinear surfaces with cracks is also investigated. As a first case, cylindrical shells with circumferential cracks are considered. Obtained meshfree results are compared with those of FEM in Table 4. It is seen from Table 4 that the correlation between the numerical results obtained by present meshfree formulation and FEM adopting different element types is good. It is noted that the buckling loads are drastically reduced with increasing the crack size. It can also be said that the buckling load of the cylindrical models is dependent on the approximation functions aside the discretization. We can see a slight difference between the results of same FEM software using different element types.

Fig.15 shows that the critical buckling mode shapes are in good agreement each other. However, the buckling modes obtained by the linear shell elements (Shell181) are not exactly symmetric while the buckling modes obtained by the present formulation and quadratic shell elements (Shell281) are

Table 4: Normalized buckling stresses L_k for circumferential crack cases.

Model	$c/2\pi r_{\mathrm{d}}$	MFree	FEM (Shell181)	FEM (Shell281)
CC1	0.05	0.370	0.346	0.338
CC2	0.10	0.162	0.151	0.145
CC3	0.15	0.070	0.063	0.061

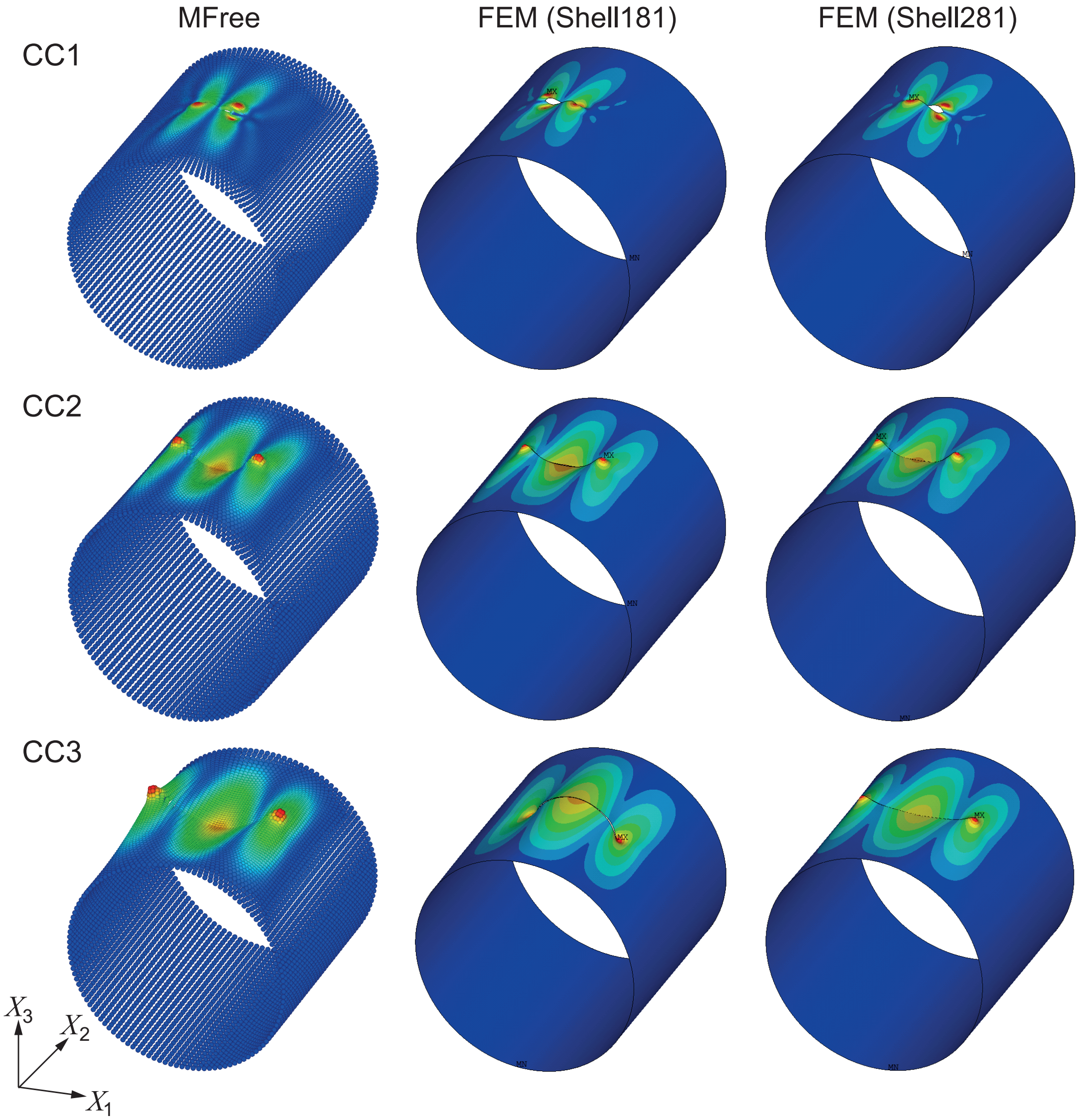

Figure 15: Comparison of the critical buckling mode shapes for the circumferential crack cases between the present meshfree method and FEM.

in agreement. In the smallest crack case, the complexity of the mode shape is obvious. This could be the reason why the differences between the numerical results for this case are relatively larger compared to the other crack sizes. The buckling modes are also complicated for the larger crack cases compared with the buckling modes of the axial cracks as shall be given later. Buckling of cylindrical shells is inherently more unstable compared to that of flat shells so that buckling modes sometimes concentrate in a narrow space and we can observe many buckling modes around a certain buckling load. This is observed for $c/2\pi r_\mathrm{d}$=0.05 and 0.15 cases by linear shell elements. In these cases, the buckling mode shapes are in reverse direction to those of meshfree and quadratic elements even if the buckling loads are in agreement. These results show that the present meshfree formulation is sometimes superior to the linear shell elements in the modeling and analysis of curvilinear surfaces with cracks.

As a second case, cylindrical shells with axial cracks are considered. Obtained results by present formulation and FEM are given in Table 5. It is seen from the Table 5 that agreement between the results is relatively better compared to the circumferential crack cases. This could be explained by the simple buckling behavior of the cylindrical shells with axial cracks as can be seen in Fig.16. Buckling loads decrease with increasing the crack size. It should be noted that the buckling loads are still much higher than those of the models with circumferential cracks. It could be said that the effect of cracks might be more destructive when the crack is located in normal to the load direction for cylindrical shells in terms of buckling consideration.

Table 5: Normalized buckling stresses L_k for axial crack cases.

Model	c/L	MFree	FEM (Shell181)	FEM (Shell281)
AC1	0.05	0.697	0.672	0.666
AC2	0.10	0.418	0.405	0.404
AC3	0.15	0.315	0.301	0.302

Present numerical results are compared with those of reference paper in Fig.17(a) and (b) for circumferential and axial crack cases, respectively. In the figure, reference results are obtained by digitizing the graphical data from the given figures of Ref. [12]. The obvious difference between the present numerical results and the reference results can be observed for circumferential crack cases, see Fig.17(a). This is because very fine discretization along the crack segment is adopted in the present numerical computations, while the

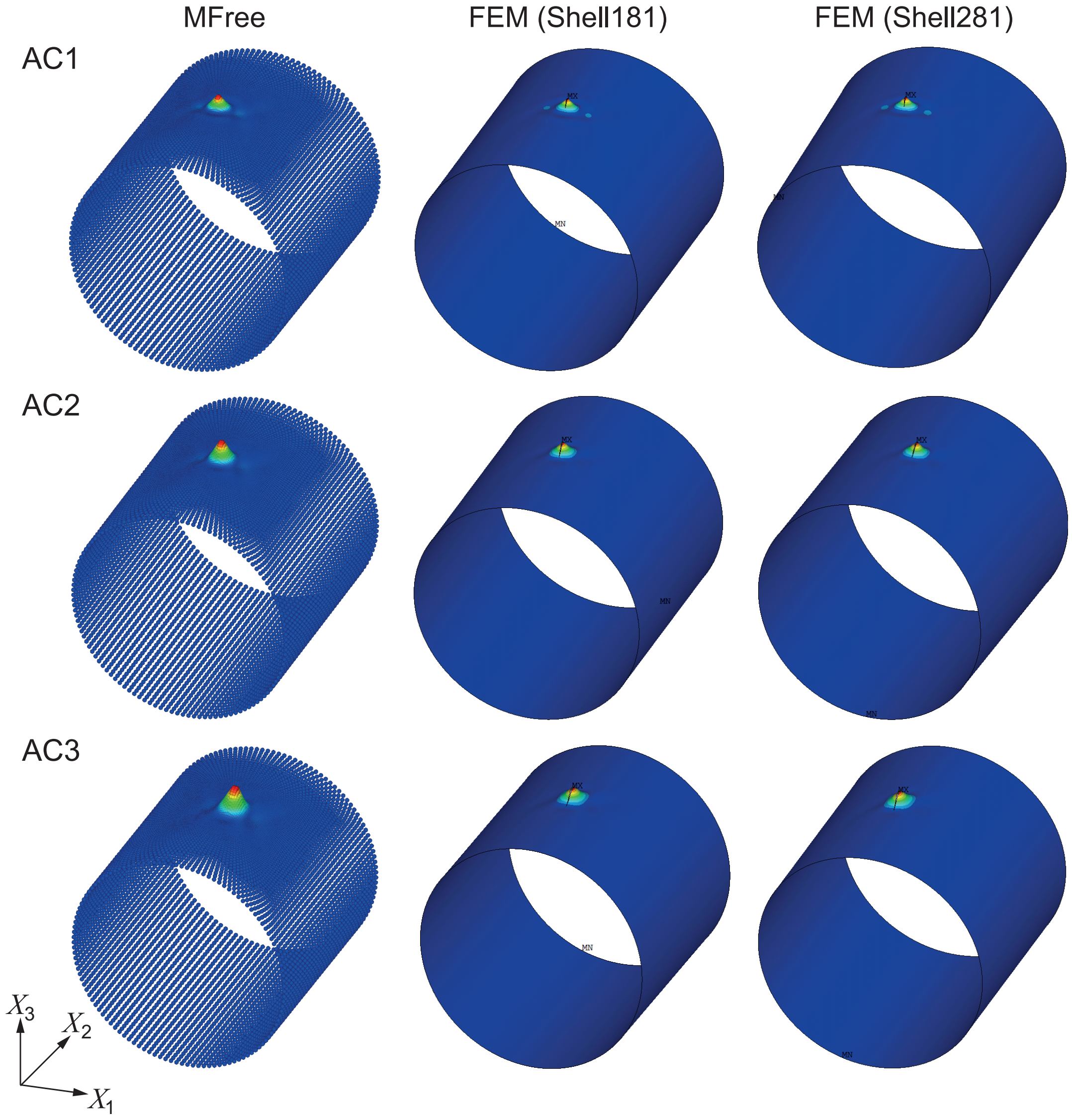

Figure 16: Comparison of the critical buckling mode shapes for the axial crack cases between the present meshfree method and FEM.

reference results have been obtained by relatively coarse mesh. For instance, 16 elements were adopted by Ref. [12] in case of $c/2\pi r_\mathrm{d}$=0.15, while we adopt 45 elements for the same crack size. As previously indicated in Fig.15, buckling modes of the cylindrical models with circumferential cracks are complicated. To simulate such complicated behavior accurately, the discretization must be fine enough. As for the cylindrical shells with axial cracks, we can observe that the reference and present numerical results are in good agreement except the smallest crack size. Since the buckling behavior is much simpler (one half-wave mode), the effect of discretization becomes less significant as the crack size becomes large. In case of the smallest crack, even if the buckling behavior is simple, the finer nodal distribution must be allocated along the crack segment to capture the buckling wave smoothly. Eight elements were adopted by Ref. [12] for axial crack problems. It is observed that eight elements could be enough for c/L=0.1 and 0.15 cases, however more elements are required for c/L=0.05 case. We adopt ten elements for the smallest crack size and more elements for the larger cracks. This could be reason of the difference between the present numerical computations and the reference results.

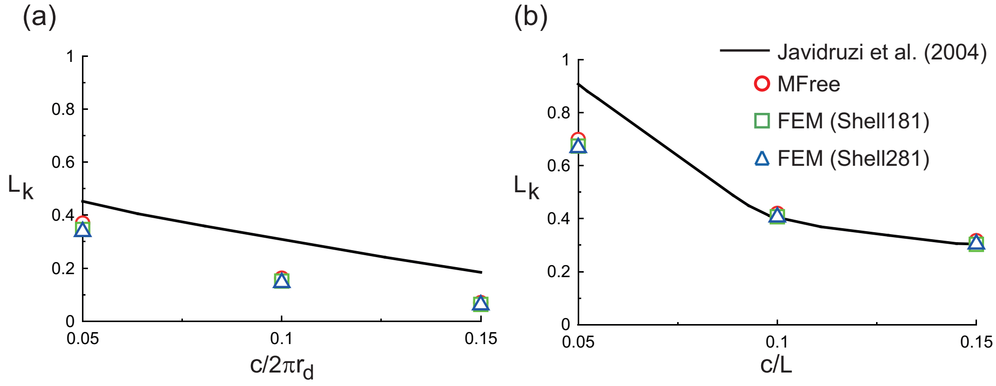

Figure 17: Comparison of critical buckling coefficients: (a) circumferential crack case, (b) axial crack case.

6. Conclusions

In this paper, numerical results of linear buckling behavior of cracked flat and cylindrical shells have been presented. The objective of the study is to show the efficiency and accuracy of the proposed meshfree RKPM in comparison with the FEM. Following comments can be made on the numerical results.

Buckling load and modes of cracked flat shells are examined and compared with those of FEM as well as reference solutions. A good agreement is achieved between the reference and numerical results. It is also interesting to see that buckling load of cracked flat shells is higher than that of intact ones when the crack is oriented in normal to the load direction. In case of flat shell models including both cutout and cracks, the correlation between the results of FEM and present formulation is also very good. Similar trend with the cracked flat shell is observed for the flat shells with cutout and crack that is the buckling load increases when the crack is oriented in normal to the load direction.

For the cracked cylindrical shells, the agreement between the numerical results is good. In those cases, the effect of element formulation is also investigated. The FEM results obtained by linear and quadratic elements are in agreement with each other in terms of buckling loads. On the other hand, buckling mode shapes obtained by present formulation sometimes become in reverse direction to those by linear shell elements, while they are in same direction with those by quadratic shell elements. The numerical results are also compared with those of reference paper in case of axial and circumferential cracks. It is observed that the reference paper overestimates the buckling loads of the cylindrical shells. This is because of that the adopted mesh scheme in the reference paper is relatively coarse compared to our numerical computations.

Although our proposed meshfree method has attractive features, both linear and quadratic FEM computations are faster than our meshfree code for same DOFs. Further investigation is required to improve not only computational efficiency but also accuracy to develop more suitable computational technique for structural analysis. Some relevant potential problems also appear worth of further investigations. For instance, the present formulation could be further improved to consider results of different crack angles for cylindrical shells; we can also extend this work to simulate the evolution of cracks in shells; or geometrical nonlinear bending of shells; buckling of cracked functionally graded shells; and so on. Some of these mentioned works have been under developments for up-coming manuscripts.

7. Acknowledgements

This research was partially supported by JSPS KAKENHI Grant-in-Aid for Scientific Research of (A)(15H02328), (B)(16H04603), (C)(15K06632).

References

[1] Tanaka S, Yanagihara D, Yasuoka A, Harada M, Okazawa S, Fujikubo M, Yao T. Evaluation of ultimate strength of stiffened panels under longitudinal thrust. Mar Struct 2014;36:21–50.

[2] Ozdemir M, Ergin A, Yanagihara D, Tanaka S, Yao T. A new method to estimate ultimate strength of stiffened panels under longitudinal thrust based on analytical formulas. Mar Struct 2018;59:510–35.

[3] Pei Z, Iijima K, Fujikubo M, Tanaka S, Okazawa S, Yao T. Simulation on progressive collapse behaviour of whole ship model under extreme waves using idealized structural unit method. Mar Struct 2015;40:104–33.

[4] Joshi PV, Jain NK, Ramtekkar GD, Virdi GS. Vibration and buckling analysis of partially cracked thin orthotropic rectangular plates in thermal environment. Thin-Walled Struct 2016;109:143–58.

[5] Pan Z, Cheng Y, Liu J. A semi-analytical analysis of the elastic buckling of cracked thin plates under axial compression using actual non-uniform stress distribution. Thin-Walled Struct 2013;73:229–41.

[6] Zeng HC, Huang CS, Leissa AW, Chang MJ. Vibrations and stability of a loaded side-cracked rectangular plate via the MLS-Ritz method. Thin-Walled Struct 2016;106:459–70.

[7] Starnes JH Jr, Rose CA. Stable tearing and buckling responses of unstiffened aluminum shells with long cracks. The Second Joint NASA/FAA/DoD Conference on Aging Aircraft 1998:610–26.

[8] Seifi R, Kabiri AR. Lateral load effects on buckling of cracked plates under tensile loading. Thin-Walled Struct 2013;72:37–47.

[9] Saad-Eldeen S, Garbatov Y, Soares CG. Experimental investigation on the residual strength of thin steel plates with a central elliptic opening and locked cracks. Ocean Eng 2016;115:19–29.

[10] Vafai A, Estekanchi HE. A parametric finite element study of cracked plates and shells. Thin-Walled Struct 1999;33:211–29.

[11] Estekanchi HE, Vafai A. On the buckling of cylindrical shells with through cracks under axial load. Thin-Walled Struct 1999;35:255–74.

[12] Javidruzi M, Vafai A, Chen JF, Chilton JC. Vibration, buckling and dynamic stability of cracked cylindrical shells. Thin-Walled Struct 2004;42:79–99.

[13] Brighenti R. Numerical buckling analysis of compressed or tensioned cracked thin plates. Eng Struct 2005;27:265–76.

[14] Vaziri A. On the buckling of cracked composite cylindrical shells under axial compression. Compos Struct 2007;80:152–8.

[15] Khedmati MR, Edalat P, Javidruzi M. Sensitivity analysis of the elastic buckling of cracked plate elements under axial compression. Thin-Walled Struct 2009;47:522–36.

[16] Seifi R, Khoda-yari N. Experimental and numerical studies on buckling of cracked thin-plates under full and partial compression edge loading. Thin-Walled Struct 2011;49:1504–16.

[17] Jahromi BH, Vaziri A. Instability of cylindrical shells with single and multiple cracks under axial compression. Thin-Walled Struct 2012;54:35–43.

[18] Allahbakhsh H, Shariati M. Instability of cracked CFRP composite cylindrical shells under combined loading. Thin-Walled Struct 2014;74:28–35.

[19] Seifi R, Googarchin HS, Farrokhi M. Buckling of cracked cylindrical panels under axially compressive and tensile loads. Thin-Walled Struct 2015;94:457–65.

[20] Baiz PM, Natarajan S, Bordas SPA, Kerfriden P, Rabczuk T. Linear buckling analysis of cracked plates by SFEM and XFEM. J Mech Mater Struct 2011;6:1213–38.

[21] Nasirmanesh A, Mohammedi S. XFEM buckling analysis of cracked composite plates. Compos Struct 2015;131:333–43.

[22] Nasirmanesh A, Mohammedi S. Eigenvalue buckling analysis of cracked functionally graded cylindrical shells in the framework of the extended finite element method. Compos Struct 2017;159:548–66.

[23] Bathe KJ. Finite element procedures. Prentice-Hall, Inc; 1996.

[24] Belytschko T, Liu WK, Moran B, Elkhodary KI. Nonlinear finite elements for continua and structures. 2nd ed. John Wiley & Sons Ltd; 2014.

[25] Bui TQ, Nguyen MN, Zhang Ch. Buckling analysis of Reissner-Mindlin plates subjected to in-plane edge loads using a shear-locking-free and meshfree method. Eng Anal Bound Elem 2011;35:1038–53.

[26] Sadamoto S, Tanaka S, Okazawa S. Elastic large deflection analysis of plates subjected to uniaxial thrust using meshfree Mindlin-Reissner formulation. Comput Mech 2013;52:1313–30.

[27] Tanaka S, Sadamoto S, Okazawa S. Nonlinear thin-plate bending analyses using the Hermite reproducing kernel approximation. Int J Comput Methods 2012;9:1240012.

[28] Wang D, Chen P. Quasi-convex reproducing kernel meshfree method. Comput Mech 2014;54:689–709.

[29] Thai CH, Nguyen TN, Rabczuk T, Nguyen-Xuan H. An improved moving Kriging meshfree method for plate analysis using a refined plate theory. Comput Struct 2016;176:34–49.

[30] Liu L, Chua LP, Ghista DN. Mesh-free radial basis function method for static, free vibration and buckling analysis of shear deformable composite laminates. Compos Struct 2007;78:58–69.

[31] Phan-Dao HH, Thai CH, Lee J, Nguyen-Xuan H. Analysis of laminated composite and sandwich plate structures using generalized layerwise HSDT and improved meshfree radial point interpolation method. Aero Sci Tech 2016;58:641–60.

[32] Roque CMC, Madeira JFA. RBF-FD meshless optimization using direct search (GLODS) in the analysis of composite plates. Eng Anal Bound Elem 2018;92:114–23.

[33] Thai CH, Do VNV, Nguyen-Xuan H. An improved moving Kriging-based meshfree method for static, dynamic and buckling analyses of functionally graded isotropic and sandwich plates. Eng Anal Bound Elem 2016;64:122–36.

[34] Vu TV, Nguyen NH, Khosravifard A, Hematiyan MR, Tanaka S, Bui TQ. A simple FSDT-based meshfree method for analysis of functionally graded plates. Eng Anal Bound Elem 2017;79:1–12.

[35] Vu TV, Khosravifard A, Hematiyan MR, Bui TQ. A new refined simple TSDT-based effective meshfree method for analysis of through-thickness FG plates. Appl Math Model 2018:57:514–34.

[36] Nguyen NT, Bui TQ, Zhang C, Truong TT. Crack growth modeling in elastic solids by the extended meshfree Galerkin radial point interpolation method. Eng Anal Bound Elem 2014;44:87–97.

[37] Liu F, Xia K. Structured mesh refinement in MLS-based numerical manifold method and its application to crack problems. Eng Anal Bound Elem 2017;84:42–51.

[38] Memari A, Azar MRK. Quick and robust meshless analysis of cracked body with coupled generalized hyperbolic thermo-elasticity formulation. Eng Anal Bound Elem 2018;90:47–62.

[39] Hughes TJR, Cottrell JA, Bazilevs Y. Isogeometric analysis: CAD, finite elements, NURBS, exact geometry and mesh refinement. Comput Meth Appl Mech Eng 2005;194:4135–95.

[40] Kiendl J, Bletzinger KU, Linhard J, Wüchner R. Isogeometric shell analysis with Kirchhoff-Love elements. Comput Meth Appl Mech Eng 2009;198:3902–14.

[41] Tran LV, Thai CH, Nguyen-Xuan H. An isogeometric finite element formulation for thermal buckling analysis of functionally graded plates. Finite Elem Anal Des 2013;73:65–76.

[42] Li X, Zhang J, Zheng Y. Static and free vibration analysis of laminated composite plates using isogeometric approach based on the third order shear deformation theory. Adv Mech Eng 2014;6:16 pgs.

[43] Yu T, Yin S, Bui TQ, Xia S, Tanaka S, Hirose S. NURBS-based isogeometric analysis of buckling and free vibration problems for laminated composites plates with complicated cutouts using a new simple FSDT theory and level set method. Thin-Walled Struct 2016;101:141–56.

[44] Alesadi A, Galehdari M, Shojaee S. Free vibration and buckling analysis cross-ply laminated composite plates using Carrera's unified formulation based on Isogeometric approach. Comput Struct 2017;183:38–47.

[45] Liu S, Yu T, Bui TQ, Yin S, Thai D-K, Tanaka S. Analysis of functionally graded plates by a simple locking-free quasi-3D hyperbolic plate isogeometric method. Compos B Eng 2017;120:182–96.

[46] Yildizdag ME, Demirtas M, Ergin A. Multipatch discontinuous Galerkin isogeometric analysis of composite laminates. Continuum Mech Therm 2018; DOI:10.1007/s00161-018-0696-9.

[47] Bhardwaj G. Singh IV, Mishra BK, Bui TQ. Numerical simulation of functionally graded cracked plates using NURBS based XIGA under different loads and boundary conditions. Compos Struct 2015;126:347–59.

[48] Yu T, Bui TQ, Yin S, Doan DH, Wu CT, Do TV, Tanaka S. On the thermal buckling analysis of functionally graded plates with internal defects using extended isogeometric analysis. Compos Struct 2016;136:684–95.

[49] Nguyen-Thanh N, Valizadeh N, Nguyen MN, Nguyen-Xuan H, Zhuang X, Areias P, Zi G, Bazilevs Y, De Lorenzis L, Rabczuk T. An extended isogeometric thin shell analysis based on Kirchhoff-Love theory. Comput Meth Appl Mech Eng 2015;284:265–91.

[50] Liu WK, Jun S, Zhang YF. Reproducing kernel particle methods. Int J Numer Meth Fluid 1995;20:1081–106.

[51] Yoshida K, Sadamoto S, Setoyama Y, Tanaka S, Bui TQ, Murakami C, Yanagihara D. Meshfree flat-shell formulation for evaluating linear buckling loads and mode shapes of structural plates. J Mar Sci Tech 2017;22:501–12.

[52] Sadamoto S, Tanaka S, Taniguchi K, Ozdemir M, Bui TQ, Murakami C, Yanagihara D. Buckling analysis of stiffened plate structures by an improved meshfree flat shell formulation. Thin-Walled Struct 2017;117:303–13.

[53] Sadamoto S, Ozdemir M, Tanaka S, Taniguchi K, Yu T, Bui TQ. An effective meshfree reproducing kernel method for buckling analysis of cylindrical shells with and without cutouts. Comput Mech 2017;59:919–32.

[54] Ozdemir M, Sadamoto S, Tanaka S, Okazawa S, Yu T, Bui TQ. Application of 6-DOFs meshfree modeling to the linear buckling analysis of stiffened plates with curvilinear surfaces. Acta Mech [accepted].

[55] Chen JS, Wu CT, Yoon S, You Y. A stabilized conforming nodal integration for Galerkin mesh-free methods. Int J Numer Meth Eng 2001;50:435–66.

[56] Chen JS, Yoon S, Wu CT. Non-linear version of stabilized conforming nodal integration for Galerkin mesh-free methods. Int J Numer Meth Eng 2002;53:2587–615.

[57] Wang D, Chen JS. A Hermite reproducing kernel approximation for thin-plate analysis with sub-domain stabilized conforming integration. Int J Numer Meth Eng 2008;74:368–90.

[58] Wang D, Lin Z. Dispersion and transient analyses of Hermite reproducing kernel Galerkin meshfree method with sub-domain stabilized conforming integration for thin beam and plate structures. Comput Mech 2011;48:47–63.

[59] Wang D, Peng H. A Hermite reproducing kernel Galerkin meshfree approach for buckling analysis of thin plates. Comput Mech 2013;51:1013–29.

[60] Wang D, Song C, Peng H. A circumferentially enhanced Hermite reproducing kernel meshfree method for buckling analysis of Kirchhoff-Love cylindrical shells. Int J Struct Stabil Dynam 2015;15:1450090.

[61] Wang D, Wu J. An efficient nesting sub-domain gradient smoothing integration algorithm with quadratic exactness for Galerkin meshfree methods. Comput Meth Appl Mech Eng 2016;298:485–519.

[62] Tanaka S, Suzuki H, Sadamoto S, Imachi M, Bui TQ. Analysis of cracked shear deformable plates by an effective meshfree plate formulation. Eng Fract Mech 2015;144:142–57.

[63] Tanaka S, Suzuki H, Sadamoto S, Sannomaru S, Yu T, Bui TQ. J-integral evaluation for 2D mixed-mode crack problems employing a meshfree stabilized conforming nodal integration method. Comput Mech 2016;58:185–98.

[64] Tanaka S, Suzuki H, Sadamoto S, Okazawa S, Yu T, Bui TQ. Accurate evaluation of mixed-mode intensity factors of cracked shear-deformable plates by an enriched meshfree Galerkin formulation. Arch Appl Mech 2017;87:279–98.

[65] Organ D, Fleming M, Terry T, Belytschko T. Continuous meshless approximations for nonconvex bodies by diffraction and transparency. Comput Mech 1996;18:225–35.

[66] Krysl P, Belytschko T. Element-free Galerkin method: Convergence of the continuous and discontinuous shape functions. Comput Meth Appl Mech Eng 1997;148:257–77.

[67] Chen JS, Wang HP. New boundary condition treatments in meshfree computation of contact problems. Comput Meth Appl Mech Eng 2000;187:441–68.

[68] ANSYS vers. 14.5; 2013.

[69] Yao T, Fujikubo M. Buckling and ultimate strength of ship and ship-like floating structures. Butterworth-Heinemann; 2016.

[70] Chen JS, Wang D. A constrained reproducing kernel particle formulation for shear deformable shell in Cartesian coordinates. Int J Numer Meth Eng 2006;68:151–72.